Spectral phase encoded time spread optical code division multiple access technology for next generation communication networks [Invited]

S. J. B. Yoo,[1,*] J. P. Heritage,[1] V. J. Hernandez,[1] R. P. Scott,[1] W. Cong,[1] N. K. Fontaine,[1] R. G. Broeke,[1] J. Cao,[1] S.-W. Seo,[1] J.-H. Baek,[1] F. M. Soares,[1] Y. Du,[1] C. Yang,[1] W. Jiang,[1] K. Aihara,[1] Z. Ding,[1] B. H. Kolner,[1] Anh-Vu Pham,[1] Shu Lin,[1] F. Olsson,[2] S. Lourdudoss,[2] K. Y. Liou,[3] S. N. G. Chu,[3] R. A. Hamm,[3] B. Patel,[3] W. S. Hobson,[3] J. R. Lothian,[3] S. Vatanapradit,[3] L. A. Gruezke,[3] W. T. Tsang,[3] M. Shearn,[4] and A. Scherer[4]

[1]*Department of Electrical and Computer Engineering, University of California, Davis, California 95616, USA*
[2]*Department of Microelectronics and Information Technology, Royal Institute of Technology, KTH-Electrum 229, S-16440 Kista, Sweden*
[3]*Multiplex, Inc., 5000 Hadley Road, South Plainfield, New Jersey 07080, USA*
[4]*Department of Applied Physics, California Institute of Technology, Pasadena, California 91125, USA*
[*]*Corresponding author: yoo@ucdavis.edu*

Received June 11, 2007; accepted July 10, 2007;
published September 14, 2007 (Doc. ID 83028)

We overview and summarize the progress of the spectral phase encoded time spreading (SPECTS) optical code division multiple access (O-CDMA) technology. Recent progress included a demonstration of a 320 Gbit/s (32-user $\times$10 Gbit/s) all-optical passive optical network testbed based on the SPECTS O-CDMA technology and a theoretical prediction of the spectral efficiency at 100% and above. In particular, InP-based integrated photonics allows implementation of SPECTS O-CDMA transmitters and receivers monolithically integrated on a chip. The integrated InP chip technology not only allows robust and compact configurations for practical and low-cost O-CDMA network deployments but also offers code reconfigurations at rapid rates for secure communication applications.
OCIS codes: 060.4080, 060.4510, 130.3120.

1. Introduction

The explosive traffic growth in the Internet has spurred deployment of optical technologies in wide-area and metropolitan-area networks (WANs and MANs). In local access networks (LANs), optical transport and switching are no longer the primary considerations, but most important issues are flexible utilization of large networking capacity as well as practical issues related to cost, complexity, and size. In addition, security enhanced by physical layer mechanisms can help alleviate complicated encryption and decryption electronics running at high speeds, especially at the boundary of LAN and MAN/WANs. Wireless code division multiple access (W-CDMA) has been a great success in LANs—unlike frequency division multiple access (FDMA) and time-division multiple access (TDMA) technologies, the W-CDMA technology was relatively immune to multipath interference noise and allowed a common set of "channels" to be deployed in neighboring cells. Consequently, rake-receivers could be deployed in W-CDMAs so that signals can be collected from all directions. The overall improvement in the bandwidth utilization and signal-to-noise ratio in W-CDMA over the competing technologies is estimated at four times or greater. In addition to the performance advantage in W-CDMA, efficient and compact W-CDMA chip development allowed rapid market-driven transition from the conventional FDMA and TDMA wireless LAN technology to the W-CDMA LAN technology.

A natural transition to the next generation LAN is to consider optical-CDMA (O-CDMA) that can potentially exploit the advantages of CDMA and the high capacity

1536-5379/07/101210-18/$15.00

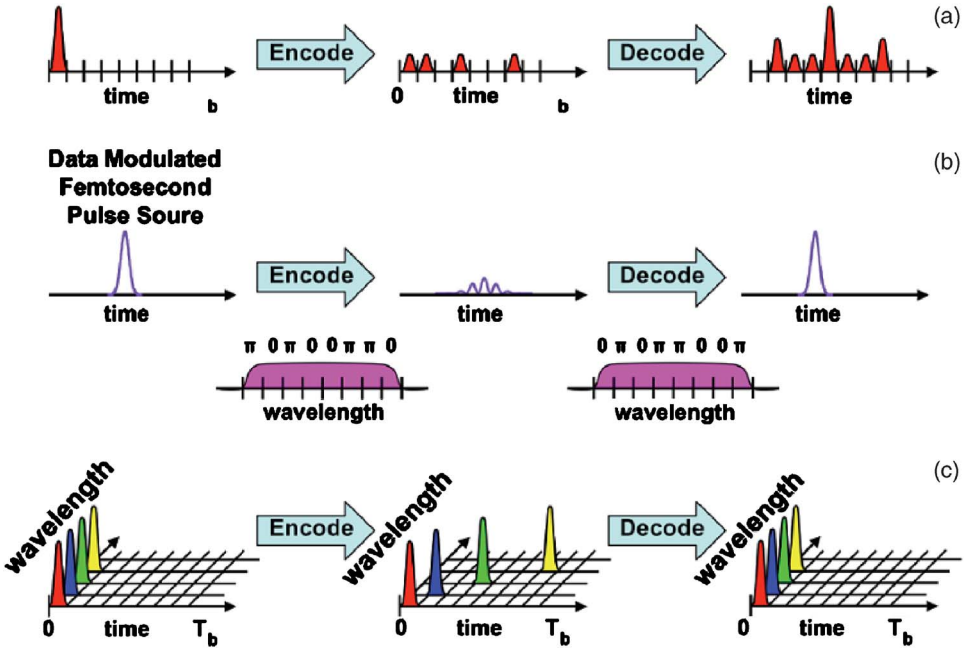

Fig. 1. Operating principles of selected O-CDMA schemes: (a) incoherent time spreading, (b) SPECTS, (c) wavelength/time coding.

of optical networks. There are significant challenges in this transition from W-CDMA to O-CDMA, primarily due to the immensely higher carrier frequency of optical waves, and also due to the practical need to develop a new optical chip for O-CDMA networking. In W-CDMA, the code is applied in the time domain, in series to the data modulation over the microwave carrier in the approximate gigahertz range. On the other hand, O-CDMA has the optical carrier frequency exceeding 100 THz, and it is difficult to achieve such a code modulation in time. Consequently, O-CDMA research investigated optical codes applied in various combinations of wavelength and time domains. Also, in O-CDMA, the fast carrier frequency allowed considerations of coherent and incoherent O-CDMA technologies. Various O-CDMA schemes fall into categories defined by coherent-versus-incoherent, synchronous-versus-asynchronous, and various coding methods in the wavelength and time domains. Figure 1 shows operation principles of three possible O-CDMA schemes: (a) incoherent time spreading [1–3], (b) spectral phase encoded time spreading (SPECTS) [4–13], and (c) two-dimensional wavelength/time coding [1,14,15]. References [16–20] provide summaries and historical perspectives of earlier O-CDMA schemes. This paper discusses the SPECTS O-CDMA technologies, systems, and networking testbed demonstrations, including development of monolithically integrated InP SPECTS O-CDMA microsystems on a chip.

2. SPECTS O-CDMA Operating Principles

SPECTS O-CDMA exploits the femtosecond pulse-shaping [5] technique. Figure 2 illustrates a pulse shaper apparatus used as (a) a SPECTS O-CDMA encoder and (b) a SPECTS O-CDMA decoder. The pulse shaper is composed of a pair of diffraction gratings, a pair of lenses, and a spatial light phase modulator (SLPM). In SPECTS O-CDMA, encoding is accomplished by phase-shifting individual slices (i.e., chips) of the optical spectrum. The encoding can exploit binary (quaternary) codes with 0 or π phase shift (0, $\pi/2$, π, or $3\pi/2$ phase shift) on each chip. This spectral phase shifting causes the pulse to spread in time by an amount proportional to the code length. To correctly decode a pulse, we apply the conjugate of the encoding code, thus reconstructing the short pulse, and doing otherwise will "incorrectly" decode the pulse. The code sets we use are quasi-orthogonal and if we decode using another code from the set, the pulse remains spread in time. A typical receiver, with a data-rate-limited bandwidth, will not distinguish between the correctly and incorrectly decoded pulses since each has comparable energy within a bit period. Therefore, it is necessary to use

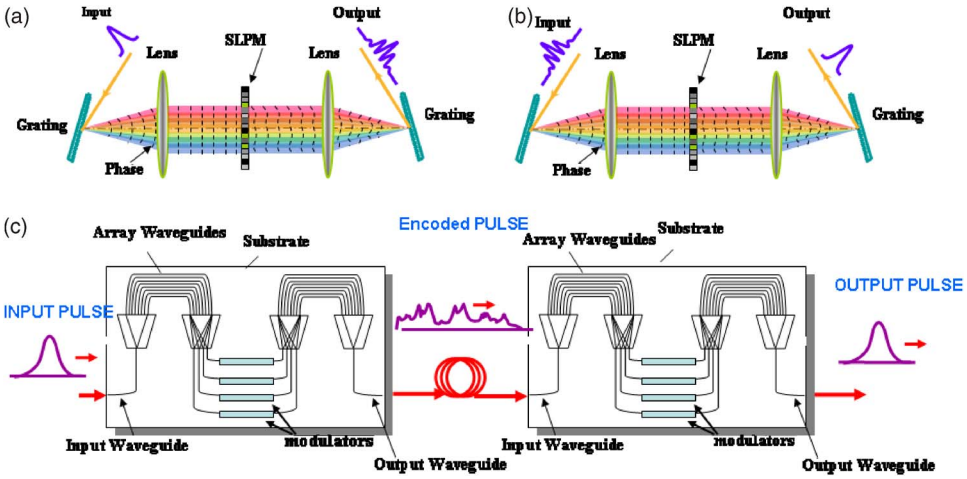

Fig. 2. Optical pulse shaping by spectral phase manipulation, exploited in the O-CDMA technology of realize (a) O-CDMA encoding, (b) O-CDMA decoding, and (c) O-CDMA encoding and decoding using InP chips employing arrayed waveguide gratings and phase modulator arrays.

either a short time gate to select out the correctly decoded pulse or a nonlinear detector that responds selectively to the high peak power of a correctly decoded pulse. Since SPECTS O-CDMA does not depend on direct-sequence encoding, the user's data rate can be variable and can increase up to the maximum rate supported by the optical network. Therefore, SPECTS is one of the most promising O-CDMA technologies for future terabit-per-second access networks.

3. SPECTS O-CDMA System and Networking Testbed

The SPECTS O-CDMA testbed consists of a zero-dispersion pulse shaper [12,13], implemented in bulk optics with fiber pigtails and the O-CDMA encoders and decoder exploiting reflective, two-dimensional, liquid-crystal spatial light phase modulators (LC-SLPMs) [14]. Figure 3 shows a diagram of the 32-user, time-slotted, polarization

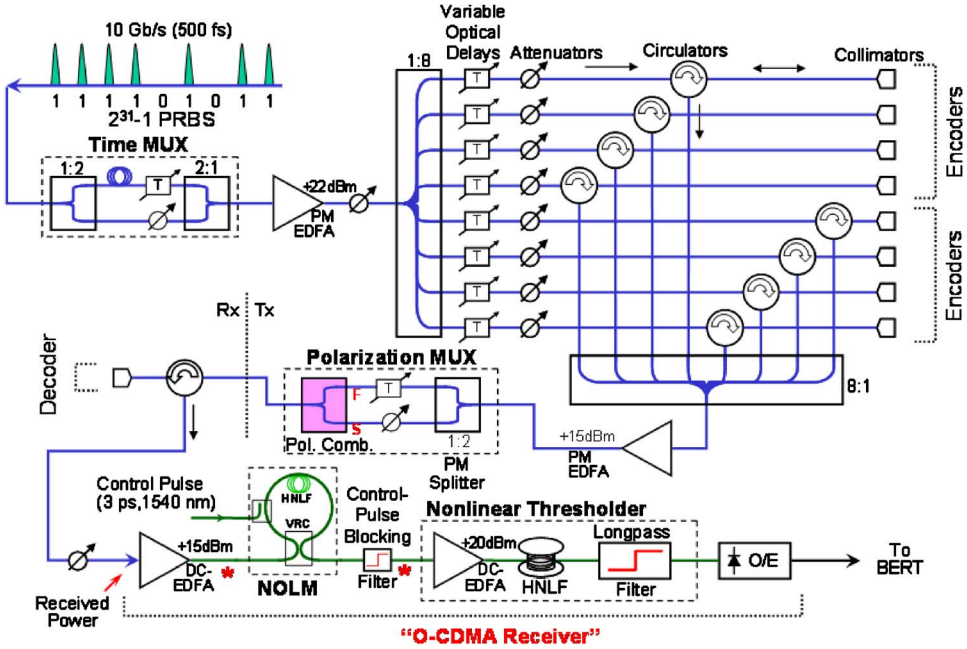

Fig. 3. Diagram of 32-user O-CDMA testbed with FEC. The experiment includes erbium-doped fiber amplifiers (EDFAs), attenuators, a pulse pattern generator (PPG), a bit error rate tester (BERT), an optical/electrical (O/E) converter, a nonlinear optical loop mirror (NOLM), highly nonlinear fiber (HNLF), a polarization beam splitter (PBS), time multiplexer (time MUX), and polarization multiplexer (polarization MUX).

multiplexed SPECTS O-CDMA testbed. A harmonically mode-locked (ML) fiber laser source running at 9.95328 Gbit/s (OC-192) generates optical pulses to be used by all O-CDMA nodes (users). The laser source consists of a ML fiber laser with an amplifier and a pulse compressor (a dispersion decreasing fiber) producing a train of 450 fs, 1 THz FWHM optical pulses. This pulse stream is modulated with a $2^{31}-1$ pseudorandom bit sequence (PRBS) before it is multiplexed into two time slots. With 9.95328 Gbit/s (OC-192) data, the time multiplexer (MUX) produces a second data set offset ~50 ps from the original, while the polarization MUX produces a separate orthogonally polarized data set. This ultimately allows up to 32 users (eight encoders × two time slots × two polarizations) to be supported on the system. We note that the system currently does not employ any transmission fiber, but transmission and recovery of femtosecond pulses (required for SPECTS) have been shown for up to 50 km of fiber [21], with actual SPECTS systems employing up to 2.5 km of fiber [9]. The eight encoders 1–8 each apply a different 64-chip Walsh code to their respective data streams, and the decoder applies a code that is the conjugate of the first encoder (Encoder 1). Therefore, the data from Encoder 1 will be correctly decoded (intended user) and the data from the other encoders will be incorrectly decoded (interfering users). Walsh codes are advantageous in the synchronous O-CDMA networking because of their property of minimizing energy from interfering users in the temporal neighborhood of the correctly reconstructed user's optical pulse, minimizing interference within the gate window. In asynchronous O-CDMA networking, *m*-sequence codes are preferred. Variable optical time delays are used to align each user's time slot to better than ±1 ps and variable attenuators are used to equalize the users' powers within ±0.2 dB. A dispersion compensated erbium-doped fiber amplifier (DC-EDFA) with 15 dBm output saturation power compensates for the optical losses before the signals go on to the decoder. Due to excess dispersion from the modulator along with residual dispersion and the spectral narrowing effects in the encoders and the decoder, the output pulse width at the decoder is typically 750–800 fs. In this setup, a nonlinear optical loop mirror (NOLM) gates one of the time slots before the nonlinear thresholder. The NOLM gate window is 3 ps (FWHM) and achieves nearly 20 dB of suppression outside the window. The pulse from the intended user is then passed through a low-noise DC-EDFA before going to the nonlinear thresholder. The thresholder uses a power DC-EDFA to amplify the signal before it goes into 500 m of highly nonlinear fiber (HNLF) (Sumitomo HNLF 1322AA-2). If the user's pulse has been correctly decoded, the high peak power of the short pulse generates a spectrum at longer and shorter wavelengths due to self-phase modulation (SPM) and other nonlinear effects in the HNLF. A long-pass filter then passes wavelengths longer than 1578 nm. The lower peak power of the incorrectly decoded pulses will not generate much additional spectrum and will be largely blocked by the long-pass filter. The typical power contrast ratio between correctly and incorrectly decoded pulses is better than 20 dB. Additional details of the thresholder operation are covered in [9,10].

3.A. Transmitter with FEC

The transmission of each user originates from a single source that consists of a ML laser followed by a data modulator. The ML laser produces 450 fs width pulses at a 9.95328 GHz repetition rate. The narrow temporal widths are necessary to create sufficient spectrum for SPECTS encoding and decoding. The pulse train is on–off keyed via a $LiNbO_3$ Mach–Zehnder modulator with an OC-192 PRBS, length (2^{31}-1), that may be optionally forward error correction (FEC) encoded using a well-known Reed–Solomon code [RS(255,239)]. When FEC is in use, the data rate is lowered to 9.250698 Gbit/s to accommodate the 6% coding overhead, maintaining the OC-192 bit rate into the modulator. The modulated light pulses are distributed between the eight O-CDMA encoders and multiplexers. Although each user's data originate from the same source, delays on each MUX and encoder path ensure that each user's data are offset by several bits. This decorrelates the PRBS between users and simulates individual data streams.

3.B. SPECTS Encoders and Decoder

The encoders and the decoder in the bulk optics O-CDMA testbed of Fig. 3 are composed of fiber pigtailed, bulk-optics-based femtosecond pulse shapers [7]. Briefly, the encoded data streams are collimated onto diffraction gratings, spatially spreading the spectral components of the incident pulses. The spread spectrum is incident upon an SLPM, which applies a phase shift to different portions of the spectrum, as designated

by the O-CDMA codes. Additional phase shifts may also be applied to help compensate for dispersion in transmission fiber [9,22]. To transfer the signal between the fiber components and bulk-optic components, collimators are employed. In the testbed, significant savings in cost and space are achieved by employing cylindrical optics and a reflective two-dimensional SLPM, as this allows multiple pulse shapers to be implemented in parallel using a single set of optics. After reflecting back into the fiber, the circulators are used to route the encoded signals through the remainder of the system. All O-CDMA-encoded data sets are combined and sent to a single decoder that applies the conjugate phase code of the desired signal. Since both the circulator and the diffraction grating of the pulse shapers are polarizing, the decoder selects the desired polarization of the polarization-multiplexed signal. Although the bulk optics of the current encoders–decoder prevent them from being used in a true telecom environment, the equivalent functions can be performed using compact arrayed waveguide gratings and phase shifters [10,23,24] depicted in Fig. 1(c).

A key to achieving high performance in the O-CDMA system is the choice of codes. In this case, 64-chip Walsh codes are chosen since they ideally produce orthogonal signals when used synchronously. The multiple access interference (MAI) produced by Walsh codes are never coincident with the correctly decoded signal, and are instead displaced to occur before or after it. This creates an interference-free window for the recovered pulse. In reality, slight irregularities in the pulse shapers cause the window to narrow, and we have thus chosen Walsh codes 5, 6, 16, 28, 34, 40, 52, and 54 for use in the encoders, since this particular subset produces an optimum window among all users. (See Table 1.) For the measurements, Walsh code 5 is used in the decoder. Attempts to optimize the receiver for detecting the other codes are currently under investigation.

Table 1. Sixty-Four-Chip Walsh Codes of the O-CDMA Testbed[a]

Number	Code (1 = π phase shift, 0 = no phase shift)
5	1 1 1 1 0 0 0 0 1 1 1 1 0 0 0 0 1 1 1 1 0 0 0 0 1 1 1 1 0 0 0 0 1 1 1 1 0 0 0 0 1 1 1 1 0 0 0 0 1 1 1 1 0 0 0 0 1 1 1 1 0 0 0 0
6	1 0 1 0 0 1 0 1 1 0 1 0 0 1 0 1 1 0 1 0 0 1 0 1 1 0 1 0 0 1 0 1 1 0 1 0 0 1 0 1 1 0 1 0 0 1 0 1 1 0 1 0 0 1 0 1 1 0 1 0 0 1 0 1
16	1 0 0 1 0 1 1 0 0 1 1 0 1 0 0 1 1 0 0 1 0 1 1 0 0 1 1 0 1 0 0 1 1 0 0 1 0 1 1 0 0 1 1 0 1 0 0 1 1 0 0 1 0 1 1 0 0 1 1 0 1 0 0 1
28	1 0 1 1 1 0 0 1 0 1 1 0 0 1 1 0 0 1 1 0 0 1 1 0 1 0 0 1 1 0 0 1 1 0 0 1 1 0 0 1 0 1 1 0 0 1 1 0 0 1 1 0 0 1 1 0 1 0 0 1 1 0 0 1
34	1 0 1 0 1 0 1 0 1 0 1 0 1 0 1 0 1 0 1 0 1 0 1 0 1 0 1 0 1 0 1 0 0 1 0 1 0 1 0 1 0 1 0 1 0 1 0 1 0 1 0 1 0 1 0 1 0 1 0 1 0 1 0 1
40	1 0 0 1 0 1 1 0 1 0 0 1 0 1 1 0 1 0 0 1 0 1 1 0 1 0 0 1 0 1 1 0 0 1 1 0 1 0 0 1 0 1 1 0 1 0 0 1 0 1 1 0 1 0 0 1 0 1 1 0 1 0 0 1
52	1 0 0 1 1 0 0 1 1 0 0 1 1 0 0 1 0 1 1 0 0 1 1 0 0 1 1 0 0 1 1 0 0 1 1 0 0 1 1 0 0 1 1 0 0 1 1 0 1 0 0 1 1 0 0 1 1 0 0 1 1 0 0 1
54	1 0 1 0 0 1 0 1 1 0 1 0 0 1 0 1 0 1 0 1 1 0 1 0 0 1 0 1 1 0 1 0 0 1 0 1 1 0 1 0 0 1 0 1 1 0 1 0 1 0 1 0 0 1 0 1 1 0 1 0 0 1 0 1

[a]Code numbers have been designated by the *Hadamard* command in MATLAB and indicate the row or column of the generated symmetric matrix.

3.C. O-CDMA Receiver

The O-CDMA receiver performs postdecoder processing of the signal and includes the thresholding function. It also contains an NOLM that serves as a time gate for selecting between the two time-multiplexed users. The NOLM switches through the desired time slot by impressing a π phase shift on the counterclockwise propagating signal, where the phase shift originates from cross phase modulation induced within the nonlinear element, 500 m of HNLF. The stimulus for cross phase modulation is a 3 ps, ~1540 nm control pulse stream with a repetition rate of 9.95328 GHz, aligned with the desired time slot. After the NOLM, the influence due to MAI is reduced by using a nonlinear thresholder, whose operating principle relies on spectral broadening resulting from SPM of incident signals within 500 m of HNLF. The correctly decoded signal will have high peak powers that can induce the spectral broadening, and these components may be filtered out and passed on to the O/E converter. MAI, with its relatively low peak power (despite having potentially high average power), will not generate spectral components within the filter's passband, and are thus suppressed. After gating and thresholding, the received signal is then FEC decoded to produce the original data stream. The O-CDMA receiver response and BER results are given in Subsection 3.D.

3.D. O-CDMA Receiver Response

Before detecting and measuring the BER of the decoded signal, the O-CDMA receiver must apply time gating (through the NOLM) and thresholding. Figure 4 shows the cross correlations of the O-CDMA signal before (gray) and after (black) the NOLM time gate. In this case, the system operates with all 32 users, but half have been deselected through polarization demultiplexing in the decoder. The remaining users distribute between two time slots in the range of −50–0 ps and 0–50 ps. Each time slot shares the same eight O-CDMA codes, so similar cross-correlation traces appear in each slot. The slight differences between their intensity levels arise from coherent interference between the various O-CDMA users. The reconstructed correctly decoded signals clearly lie at ±25 ps, and, as characteristic of the Walsh codes, they are surrounded by the MAI. The NOLM temporally gates the desired time slot, and the black trace of Fig. 5 shows the resulting output. The NOLM, with its 3 ps window, successfully passes the desired time slot while significantly suppressing the majority of MAI. The time gate is not ideal, however, in that MAI occurring within the 3 ps window still exits. Additionally, residue from the rejected time slot leaks through the NOLM and can be seen at −25 ps. The nonlinear thresholder following the NOLM suppresses this leakage and remaining MAI, since the NOLM leakage is unable to generate self-phase modulation in the nonlinear thresholder. The thresholder is thus able to produce a contrast ratio of greater than 20 dB in the 32-case.

3.E. BER Performance Comparison Using FEC

After time gating and thresholding, the signal is sent into the O/E converter for BER measurements. Figure 5(b) shows the results obtained with FEC in comparison to the results without FEC in Fig. 5(a) [25]. The independent axis indicates the received

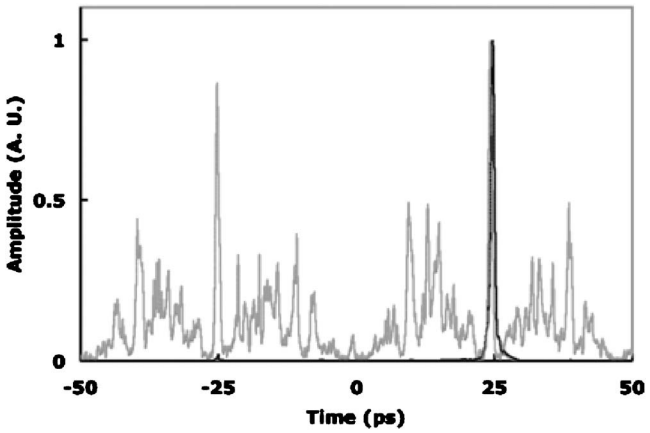

Fig. 4. Cross correlations of the O-CDMA signal before (gray) and after (black) the NOLM time gate.

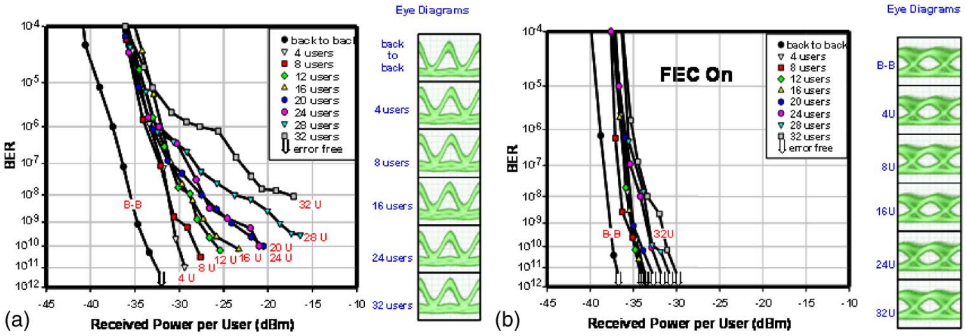

Fig. 5. Bit error rates (BERs) for the 32-user O-CDMA system (a) without and (b) with FEC [9].

power per user incident upon the O-CDMA receiver, which contains the NOLM, optical thresholder, the O/E converter, and the optional FEC decoder. BER traces are obtained from 4 to 32 users, where an encoder is added to the system for each trace. Since each encoder contains two time-division multiplex (TDM) time slots and two polarizations, four 10 Gbit/s users are added to the system per encoder. For measurements without FEC [Fig. 5(a)], the FEC encoder and FEC decoder are removed from the system, and the testbed performs at BER $<10^{-9}$ for up to 28 users. A noise floor builds with each added encoder, such that the 32-user case achieves only BER $<10^{-8}$. The noise floor largely results from coherent beat interference that occurs between the signal and any coincident MAI, and it is present regardless of MAI thresholding. With the addition of FEC [Fig. 5(b)], the BER immediately improves such that all 32 users can remain error free for a period of at least 240×10^{9} bits (BER $<10^{-11}$). The arrows at the final points of each BER curve indicate the power at which this error-free point was observed. Significantly, no error floor is evident for 32 users, suggesting that many more users could be added to the system before excessive coherent beat noise overcomes the FEC. Without FEC, the power per user clearly increases from −30.7 to −18.7 dBm going from 4 to 28 users, or a 22 dB penalty. With the FEC, sensitivity improves such that the power per user does not notably increase until going from 28 to 32 users (a 2.7 dB increase). Before this point, the power per user merely fluctuates between −36 dBm (eight users) to −33.4 dBm (28 users), a 2.6 dB range. The fluctuation, which is also evident without FEC, may be a manifestation of the wide BER variance that can be expected in a beat-noise-limited coherent O-CDMA system [26].

4. SPECTS O-CDMA Architectures, Protocols, and Performance Simulations

The synchronous SPECTS O-CDMA system has been shown to outperform the asynchronous counterpart by providing higher capacity and lower bit error rates [27–29]. Here we limit our analysis to a synchronous system. For on–off-keyed modulation, the E field received by the ith decoder can be written as [30]

$$\epsilon^{i}(t)=\frac{b^{i}}{2\pi}\sum_{n=1}^{N}\int_{\Omega_{n-1}}^{\Omega_{n}}E^{i}(\omega)e^{j\omega t}\mathrm{d}\omega+\frac{1}{2\pi}\sum_{m=1,m\neq i}^{M}b^{m}\sum_{n=1}^{N}\int_{\Omega_{n-1}}^{\Omega_{n}}E^{m}(\omega)e^{j\phi_{n}^{m}}e^{-j\phi_{n}^{i}}e^{j\omega t}\mathrm{d}\omega,\qquad(1)$$

where $b^{m}=\{0,1\}$ is the data bit sent by the mth encoder, Ω_{n} is the upper bound of the nth frequency component (chip), N is the total number of frequency chips, M is the total number of users, $E^{m}(\omega)$ is the continuous time Fourier transform (CTFT) of the temporal function of the original ultrashort pulse, and $C_{n}^{m}=e^{j\phi_{n}^{m}}$ the phase code (where ϕ_{n}^{m} is the phase shift amount) applied to the nth frequency chip by the mth encoder. The first term is the recovered short pulse from the intended sender (the ith encoder); the second term is the multiuser interference (MUI). Minimizing the MUI term is essential in the designing of the O-CDMA system, since the accumulation of MUI leads to detection errors.

Previous theoretical analyses assumed that the subpicosecond pulse possesses an ideal uniform spectrum or a constant CTFT response ($E^{m}(\omega)=E_{0}$) [2,8]. Therefore, it is

natural to move $E^m(\omega)$ out of the integration summation in Eq. (1) and, without loss of generality, set the decision point at $t=0$. Thus, the field contribution from the MUI becomes

$$\epsilon^i_{\mathrm{MUI}}(0)=\frac{E_0}{2\pi}\sum_{m=1,m\neq i}^{M} b^m\sum_{n=1}^{N} C_n^m C_n^{i*}\int_{\Omega_{n-1}}^{\Omega_n}\mathrm{d}\omega=\frac{E_0}{2\pi}\Delta\Omega\sum_{m=1,m\neq i}^{M} b^m\sum_{n=1}^{N} C_n^m C_n^{i*}, \tag{2}$$

where $\Delta\Omega=\Omega_n-\Omega_{n-1}$ is the uniform frequency chip size. Also, if the code set $\{C\}$ is orthogonal, then $\Sigma_n C_n^m C_n^{i*}=0$ for $m\neq i$ and the MUI term reduces to zero. This analysis shows that under the conditions of ideal uniform spectrum, single point detection, and orthogonal code set, one can achieve the elimination of the MUI.

Although it is difficult to perform single point detection at $t=0$ without ultrafast electronics, a narrow time gate centered at the decision point can approximate its effect [9]. Such gating can preserve all of the energy from a correctly decoded pulse while suppressing most of the energy from the MUI. All simulations in this paper have incorporated such a time gate to suppress the MUI. Furthermore, the orthogonal condition for the phase code can be achieved by the selection of either an orthogonal code set (e.g., Walsh codes) or a quasi-orthogonal code set (e.g., cyclic shifted m sequences). However, optical pulses with a uniform spectrum are uncommon in reality. Hence the orthogonality condition eliminating the MUI may no longer hold for pulses with a nonideal spectrum, leading to performance degradations. Our SPECTS O-CDMA testbed [9] utilizes a fiber compressed mode-locked laser as the ultrashort optical pulse source, and due to nonlinearity, the spectrum of its output pulses exhibits features of a complex structure, such as spikes, which will cause performance degradation due to the loss of orthogonality.

5. Nonuniform Encoding Results

To improve the performance of SPECTS O-CDMA systems with a nonideal pulse spectrum [7], we propose a novel nonuniform encoding scheme [31]. In Eq. (1), we observed that, if $\int_{\Omega_{n-1}}^{\Omega_n} E^m(\omega)\mathrm{d}\omega=I_0=$constant, the MUI term becomes

$$\epsilon^i_{\mathrm{MUI}}(0)=\frac{I_0}{2\pi}\sum_{m=1,m\neq i}^{M} b^m\sum_{n=1}^{N} C_n^m C_n^{i^*},$$

thus the orthogonality condition described in Section 4 continues to hold.

Since both our simulation and experimental realization of O-CDMA encoding are done in the discrete format in which each frequency chip consists of either a set of points (as in simulations) [7] or a group of pixels (as in experiments) [9], it is convenient to use discrete notations here. After an approximation of the integration in Eq. (1), the MUI term can be expressed as [31]

$$\epsilon^i_{\mathrm{MUI}}(0)=\frac{1}{2\pi}\sum_{m=1,m\neq i}^{M} b^m\sum_{n=1}^{N} C_n^m C_n^{i^*}\sum_{l=l_{n-1}+1}^{l_n} E_l^m\cdot\delta\omega, \tag{3}$$

where E_l^m is the E-field spectral amplitude of the lth point (pixel), l_n is the upper pixel index of the nth frequency chip, and $\delta\omega$ is the frequency pixel width. We approximate the electrical field amplitude in each frequency chip with its average value. Thus, Eq. (4) can be approximated by [31]

$$\epsilon^i_{\mathrm{MUI}}(0)\approx\frac{1}{2\pi}\sum_{m=1,m\neq i}^{M} b^m\sum_{n=1}^{N} C_n^m C_n^{i^*}\overline{E_n^m}\sum_{l=l_{n-1}+1}^{l_n}\delta\omega=\frac{1}{2\pi}\sum_{m=1,m\neq i}^{M} b^m\sum_{n=1}^{N} C_n^m C_n^{i^*}\overline{E_n^m}\cdot L_n\cdot\delta\omega, \tag{4}$$

where $L_n=l_n-l_{n-1}$ is the width in terms of pixels of the nth frequency chip. It is clear that, if we choose the width of each frequency chip according to its average E-field amplitude to make $\overline{E_n^m}L_n=$constant, then Eq. (4) can be rewritten as [31]

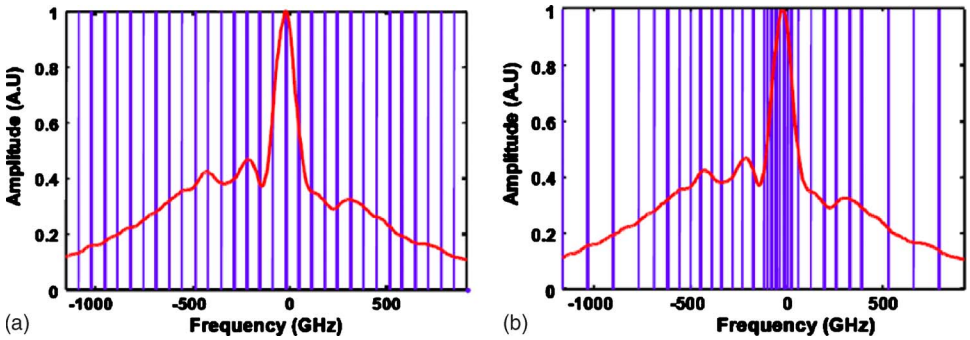

Fig. 6. Illustration of the (a) uniform and (b) nonuniform division of a measure ML laser pulse spectrum. The spectrum is divided into 31 "chips" in both figures. The frequency is offset by the carrier frequency of 193.55 THz [31].

$$\epsilon^i_{\mathrm{MUI}}(0) \approx \frac{1}{2\pi} \times \text{constant} \times \delta\omega \times \sum_{m=1,m\neq i}^{M} b^m \sum_{n=1}^{N} C_n^m C_n^{i^*}. \tag{5}$$

As analyzed in Section 2, the orthogonal condition for $\{C\}$ leads to $\Sigma_{n=1}^{N} C_n^m C_n^{i^*} = 0$ for $m \neq i$; therefore, the MUI will reduce to approximately zero.

The key to reducing the MUI with the use of this nonuniform encoding scheme is to vary the value of L_n according to the value of $\overline{E_n^m}$, such that $\overline{E_n^m} L_n = \text{constant}$, whereas the traditional uniform encoding scheme as shown in Fig. 6(a) keeps L_n constant. The full compensation of a complex spectrum often requires a rather complex scheme (N possible different values of L_n) that is hard to implement in practical systems, since N could be well over 100. A more practical approach should balance between complexity and effective compensation by the selection of a nonuniform encoding method that involves a small number of different values for L_n. Figure 6(b) shows an example of the use of five different levels of L_n to make $\overline{E_n^m} L_n$ roughly constant. Smaller L_n values are chosen for frequency chips with higher amplitudes (the center chips) and larger L_n values for those with lower amplitudes (the edge chips), as expected. The horizontal axis is in reference to the 193.55 THz optical carrier frequency.

Experimental and simulation results indicate that this new nonuniform encoding scheme, as shown in Fig. 7(b), indeed improves the performance of a SPECTS O-CDMA system [31]. Figure 7 shows a qualitative comparison between the uniform and nonuniform schemes by comparison of one MUI waveform resulting from the encoding and decoding of a pulse with 64-bit Walsh codes 5 and 53, respectively. One can easily observe that the interference level at the decision point ($t=0$) drops dramatically for the nonuniform case [Fig. 7(b)] [31]. The solid curves are simulated waveforms, and the dashed curves are cross-correlation traces obtained from the SPECTS O-CDMA testbed [9]. The simulation results agree well with the experimental SPECTS O-CDMA users, significantly enhancing the system capacity by allowing more users.

Larger-scale simulations in the context of O-CDMA networks can estimate the amount of interference in the network and thus provide statistical estimates of BERs

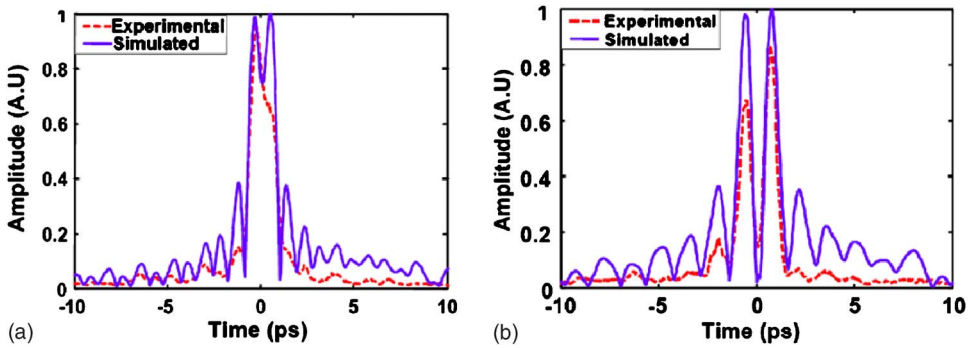

Fig. 7. Simulated (solid) and experimentally obtained (dashed) amplitude of interference (incorrect decoding) waveforms for (a) the uniform and (b) the nonuniform encoding schemes [31].

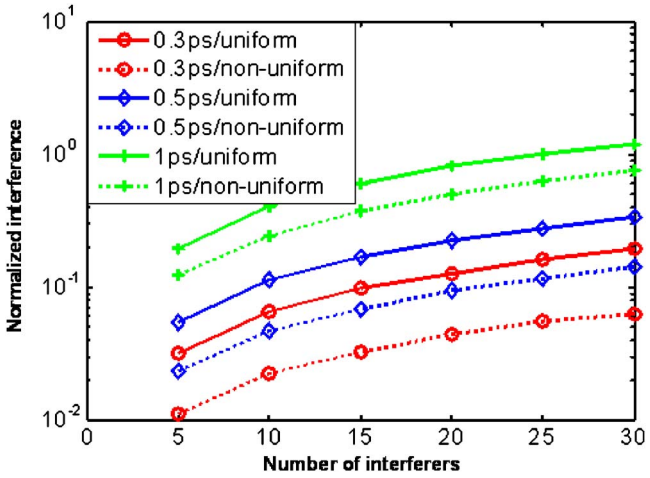

Fig. 8. Accumulated interference from interferers for uniform and nonuniform encoding schemes. The time gates are set at 0.3, 0.5, and 1 ps and the phase codes are 31-bit cyclic shifts of an m sequence [31].

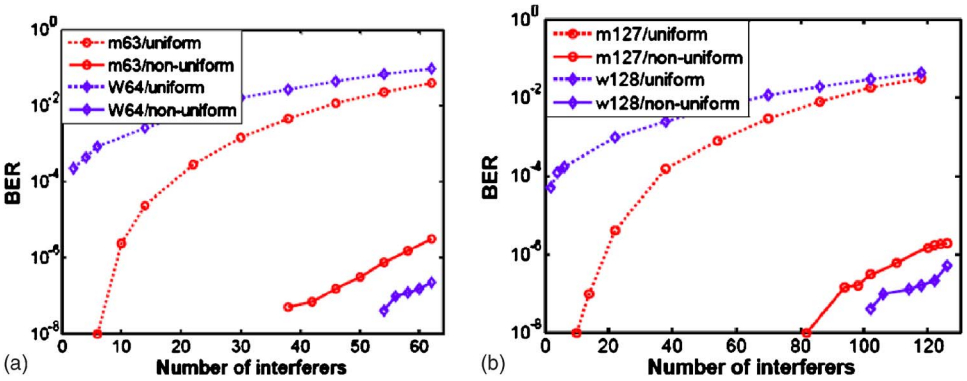

Fig. 9. BER due to interferers in uniform and nonuniform encoding schemes. The phase codes applied are (a) cyclic shifts of a 63-bit m sequence and 64-bit Walsh code, (b) cyclic shifts of a 127-bit m sequence and 128-bit Walsh code [31].

Table 2. Calculated Spectral Efficiency for Synchronous SPECTS O-CDMA

	Synchronous SPECTS O-CDMA							
	Sequential Code Assignment				Random Code Assignment			
	With/Polarization Multiplexing		Without/Polarization Multiplexing		With/Polarization Multiplexing		Without/Polarization Multiplexing	
	Uniform Coding	Nonuniform Coding	Uniform Coding	Nonuniform Coding	Uniform Coding	Nonuniform Coding	Uniform Coding	Nonuniform Coding
Without FEC	0.73 (W128/62 users, BER 1×10^{-8})	0.99 (W128/84 users, BER 1×10^{-8})	0.62 (W128/53 users, BER 1×10^{-8})	0.92 (W128/78 users, BER 1×10^{-8})	0.28 (m31/24 users, BER 1×10^{-8})	0.85 (W32/72 users, BER 1×10^{-8})	0.14 (m31/12 users, BER 1×10^{-8})	0.80 (W32/68 users, BER 1×10^{-8})
With RS[a]FEC	1.56 (W128/142 users, BER 1×10^{-9})	1.94 (W32/176 users, BER 1×10^{-9})	1.32 (W32/120 users, BER 1×10^{-9})	1.41 (W32/128 users, BER 1×10^{-9})	0.62 (m31/56 users, BER 1×10^{-9})	1.41 (W64/128 users, BER 1×10^{-9})	0.52 (m31/44 users, BER 1×10^{-9})	1.41 (W64/128 users, BER 1×10^{-9})
With LDPC[a] FEC	1.66 (W32/176 users, BER 1×10^{-9})	2.41 (W32/256 users, BER 1×10^{-9})	1.20 (W128/127 users, BER 1×10^{-9})	1.19 (W32/128 users, BER 1×10^{-9})	0.68 (m31/72 users, BER 1×10^{-9})	1.20 (W64/128 users, BER 1×10^{-9})	0.56 (m31/60 users, BER 1×10^{-9})	1.20 (W64/128 users, BER 1×10^{-9})

[a]RS is Reed–Solomon, LDPC is low-density parity check coding.

Table 3. Calculated Spectral Efficiency for Asynchronous and Random Code-Assignment SPECTS O-CDMA

	Asynchronous, Random Code-Assignment SPECTS O-CDMA			
	With Polarization Multiplexing		Without Polarization Multiplexing	
	Uniform Coding	Nonuniform Coding	Uniform Coding	Nonuniform Coding
Without FEC	0.07 (m127/6 users, BER$\times 10^{-8}$)	0.07 (m127/6 users, BER$\times 10^{-8}$)	0.05 (m127/4 users, BER$\times 10^{-8}$)	0.05 (m127/4 users, BER$\times 10^{-8}$)
With RS[a] FEC	0.22 (m127/20 users, BER$\times 10^{-9}$)	0.24 (m127/22 users, BER$\times 10^{-9}$)	0.22 (m127/20 users, BER$\times 10^{-9}$)	0.23 (m127/21 users, BER$\times 10^{-9}$)
With LDPC[a] FEC	0.28 (m127/30 users, BER$\times 10^{-9}$)	0.30 (m127/32 users, BER$\times 10^{-9}$)	0.30 (m127/32 users, BER$\times 10^{-9}$)	0.30 (m127/32 users, BER$\times 10^{-9}$)

[a]RS is Reed-Solomon, LDPC is low-density parity check coding.

in the O-CDMA networks under various schemes (synchronous versus asynchronous, etc.). Figure 8 shows normalized from interferers for uniform and nonuniform encoding schemes. The time gates are set at 0.3, 0.5, and 1 ps and the phase codes are 31-bit cyclic shifts of an m sequence [31]. Figure 9 shows BER due to interferers in uniform and nonuniform encoding schemes. The phase codes applied are (a) cyclic shifts of a 63-bit m sequence and 64-bit Walsh code, (b) cyclic shifts of a 127-bit m sequence and 128-bit Walsh code [31]. Table 2 shows estimated spectral efficiency for synchronous SPECTS O-CDMA networks, and Table 3 summarizes the same for asynchronous SPECTS O-CDMA networks.

6. Integrated SPECTS O-CDMA Technologies

The SPECTS O-CDMA discussions so far involved experiments with bulk optics and simulations assuming ideal components. It is imperative that we realize integrated and compact O-CDMA systems for robust and low-cost operation of O-CDMA networks. As illustrated in Fig. 1(b), the optical encoding and decoding in SPECTS O-CDMA can take place in a pair of arrayed waveguide gratings (AWGs) with a phase modulator array. A SPECTS O-CDMA "transmitter" will include a femtosecond laser source (e.g., a mode-locked laser), and a SPECTS O-CDMA "receiver" will include a threshold detector. In the context of a synchronous SPECTS O-CDMA, it is possible to pursue the monolithically integrated SPECTS O-CDMA "transceiver" shown in Fig. 10. Here, the monolithic integration [32] involves a colliding pulse ML laser (CPM) [33,34] and a set of AWG-phase modulator-AWG encoders as the transmitter, and

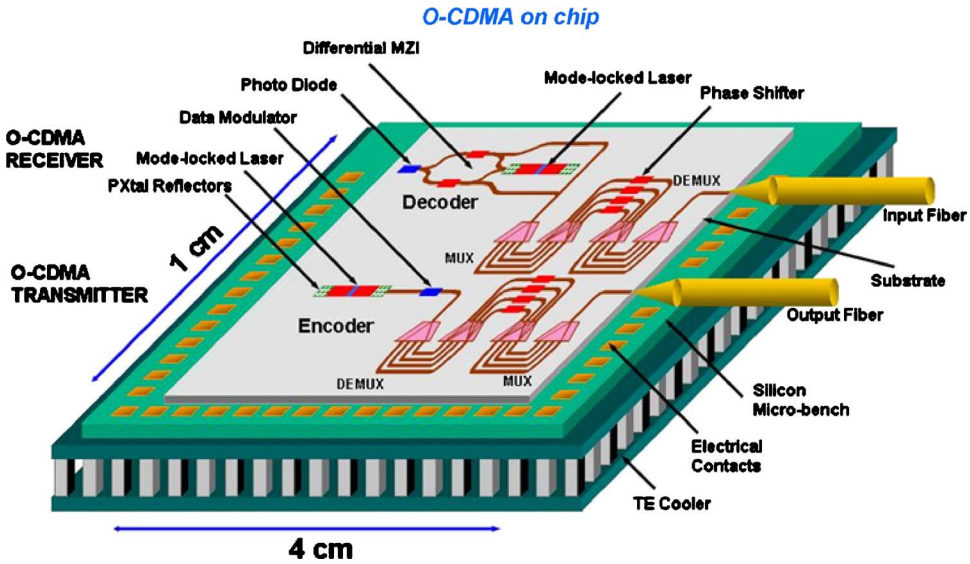

Fig. 10. Schematic of a monolithically integrated O-CDMA transceiver system.

another set of AWG-phase modulator-AWG decoders and differential Mach–Zehnder interferometric switches driven by a synchronized CPM as the receiver [35]. This section discusses demonstration and integration of individual components fabricated using a common set of fabrication processes.

6.A. ML Laser

Standard 10 GHz InP ML lasers [36] exploited the all-active linear cavity of ~4.3 mm length. For CPM lasers, the cavity length becomes ~8.6 mm, and the CPM laser will exploit an active–passive laser configuration to avoid high operating currents. Furthermore, long (>4 mm) all-active mode ML lasers for achieving lower repetition rate tend to suffer from strong pulse-shaping effects, resulting in poor chirping and jitter performance. Figure 11 shows a scanning electron micrograph (SEM) of a monolithically integrated InP CPM with active quantum well and bulk waveguide integration [33,34,37]. Unlike standard ML lasers, the CPM laser operates in the configuration where two symmetrically counterpropagating pulses collide and bleach the saturable absorber located at the center of the laser cavity, resulting in deeper saturation and more stable ML.

Adopting the active–passive integration process allows for reducing the active section length to minimize these effects and the drive current requirement [37]. The active–passive interfaces are designed to be laterally tilted at 45° relative to the waveguide direction [35]. This lateral tilt is critical for eliminating unwanted secondary pulses originating from residual reflections at the interfaces, resulting in much improved ML performance compared to the untilted designs. The active region has a total length of 2000 μm, dividing into two gain sections and sandwiching the 45 μm wide saturable absorber (SA) located at the center. The waveguide is further extended symmetrically on both sides with passive sections, forming the 8200 μm long laser cavity.

The CPM laser can be synchronized to an external system clock through either electrical hybrid mode-locking (HML) [37–39] at the fundamental or a subharmonic frequency, or through the optical synchronous mode locking (OSML) approach [40,41]. In the electrical HML configuration, the rf modulation signal is applied to the saturable absorber of the CPM laser through a ground-signal-ground microwave probe, while the two gain sections and the SA are dc biased through dc needle probes (forward current injection) and the microwave probe (reverse bias voltage) through a bias-tee connection, respectively.

CPM laser output pulse characteristics are very sensitive functions of the dc biasing and rf modulation conditions. The characterization process included the cross-correlation frequency-resolved optical gating (XFROG) technique [42] for accurate extraction of the complete temporal amplitude and phase information, and the corresponding spectral domain profiles of the pulse simultaneously.

The electrical HML investigation of the 10 GHz CPM laser is discussed in detail in [43]. Application of the rf signal with its frequency matching the passive ML frequency of 10.3 GHz at 19 dBm, we obtained nearly transform limited output with pulse width of 1.75 ps and time-bandwidth product 0.33, with relatively low timing jitter. Control devices fabricated in the same manner with standard 90° interface showed far inferior pulses with time-bandwidth product value exceeding 0.45, indicating the importance of minimizing the active–passive interfacial reflections.

In an O-CDMA network, it is far easier to achieve synchronization by optical clock distribution than to supply the rf clock signal to the electrical HML-approach-based CPM lasers. A simple master clock can supply synchronous clock signals to individual nodes with CPM lasers to achieve OSML for all lasers in all nodes simultaneously. To

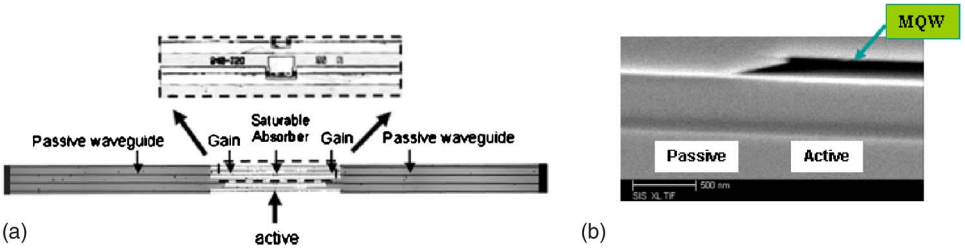

Fig. 11. SEM image of a 10 GHz CPM laser with integrated active–passive waveguide.

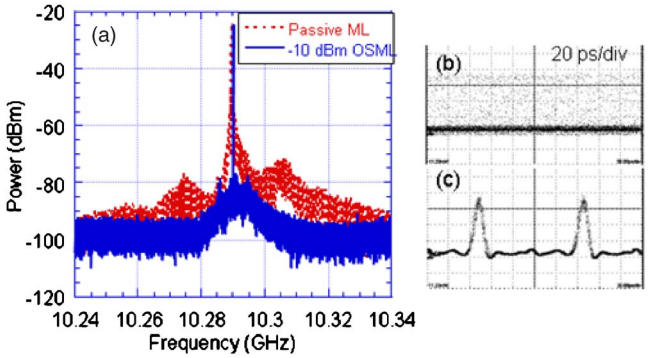

Fig. 12. (a) rf power spectra at the fundamental ML frequency of the 10 GHz CPM laser under passive ML and optical injection locking conditions. Also sampling scope traces of the CPM laser output triggered with the rf clock source under (b) passive and (c) optical injection locking conditions.

characterize OSML, a commercial tunable ML fiber laser synchronized to an rf synthesizer clock source provides the optical clock, which is coupled into the 10 GHz CPM laser through a polarization-maintaining (PM) attenuator and a lensed fiber. The CPM output, collected through a lensed fiber from the other output facet, passes through a 3 nm tunable filter for removing any residuals of the injection signal, and then routes to different instruments for time- and frequency-domain measurements, and the BERT for BER measurements.

Figure 12(a) shows the rf power spectra of a 10 GHz CPM laser under both passive ML and injection locking conditions at −10 dBm coupled optical power, with the injection signal at 1546 nm, 8 nm negatively detuned from the passive ML wavelength. Figures 12(b) and 12(c) show the corresponding 50 GHz optical sampling scope traces, triggered with the rf synthesizer clock. Compared to passive ML the rf spectral line shape narrows significantly in Fig. 12(a) under optical injection, corresponding to the sharply reduced timing jitter after synchronization. The estimated RMS timing jitter of the injection-locked CPM laser is 0.5 ps by integrating the single-sideband (SSB) phase noise spectrum, while the injected laser clock signal has rms jitter of 0.17 ps. The experiments showed the optical phase synchronization effects observed at an injection power level as low as −23 dBm. BER measurements also indicated that the CPM output is error-free with BER $< 10^{-10}$ under PRBS $2^{23}-1$ data modulation, demonstrating that the optical injection-locked 10 GHz CPM laser can indeed serve as a viable short pulse light source in high-performance O-CDMA networks.

6.B. InP Encoder and Decoder

InP SPECTS O-CDMA encoders and decoders offer rapid code reconfiguration by employing electro-optical phase shifters and the possibility of realizing monolithically integrated O-CDMA transmitters and receivers including CPM lasers and Mach–Zehnder threshold detectors [35].

Figure 13(a) shows the O-CDMA encoder mask layout. The AWG pair performs spectral demultiplexing and multiplexing. Phase modulators between the AWGs apply a phase shift corresponding to the desired O-CDMA code to each demultiplexed spectral channel. The input and output waveguides of the device are chosen for optimal wavelength match of the two AWGs. Figure 13(b) shows the packaged InP O-CDMA chip, Fig. 13(c) shows the wire-bonded InP O-CDMA chip in the package, and Fig. 13(d) shows the optical transmission spectrum through the packaged chip. The InP O-CDMA encoder (decoder) devices each consist of an identical pair of eight-channel AWGs with 180 GHz channel spacing and a free spectral range (FSR) of 12-channel spacings. The 1.4 THz wavelength span provided by the eight channels is sufficient for encoding subpicosecond (~0.5 ps) pulses. The InP devices are packaged in a standard 14-pin butterfly package with temperature control, which allows for an exact wavelength match of the encoder and decoder. The 2000 μm long phase shifters are controlled by electrically biasing wire-bonded electrical leads.

We selected the eight-chip Walsh code set for our spectral phase coding experiment involving cascaded stages of an InP encoder and an InP decoder. The InP encoder applies code W5 containing the bits [11110000], whereas the InP decoder applies conjugate code $(^{*})W5^{*}$=[00001111]. Here 1 denotes π rad phase shift and 0 denotes 0

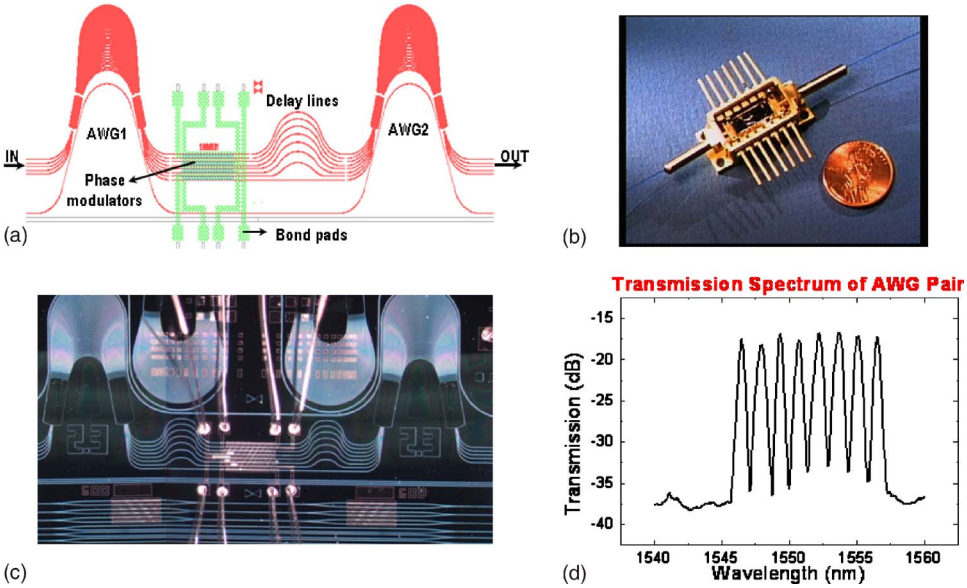

Fig. 13. (a) O-CDMA encoder (decoder) chip layout, (b) packaged O-CDMA encoder (decoder) chip, (c) fabricated InP O-CDMA encoder (decoder) chip with wire bonding, and (d) packaged O-CDMA encoder (decoder) chip transmission spectrum.

phase shift for the respective phase shifters. Figure 14 shows cross-correlation traces of (a) the cascaded encoder–decoder output with only phase error compensation applied to the phase modulators, (b) the encoder output under W5 encoding, (c) the decoder output for correctly decoded signal, and (d) the decoder output for the incorrectly decoded signal. (Solid curves are experimental results and dotted curves are simulated results.) The results indicate a clear contrast between the correctly decoded

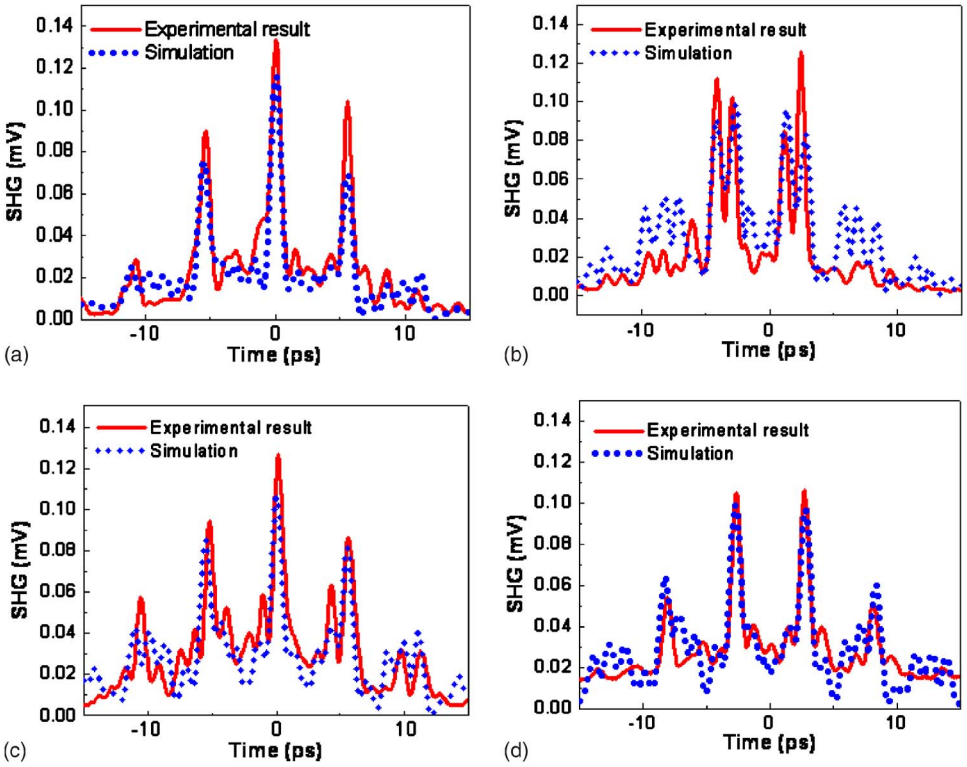

Fig. 14. Cross-correlation traces of (a) cascaded encoder–decoder output with only phase error compensation applied to the phase modulators, (b) encoder output under W5 encoding, (c) decoder output for the correctly decoded signal, and (d) decoder output for incorrectly decoded signal. Solid curves are experimental results and dotted curves are simulated results. W5 code is [11110000].

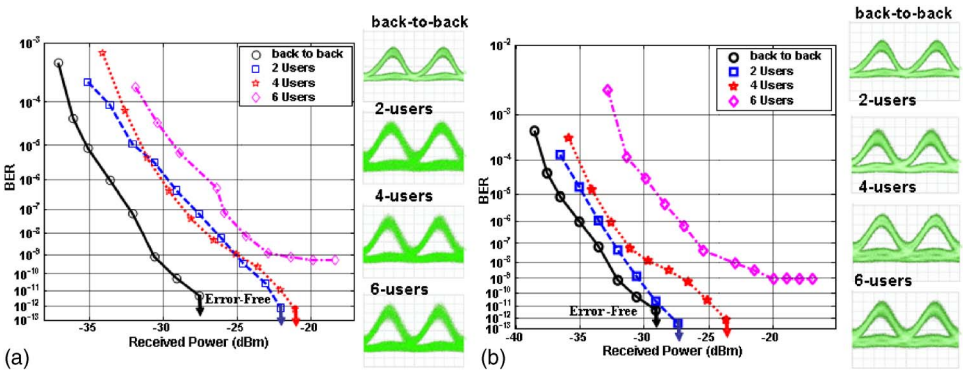

Fig. 15. BER measurement results for ER measurement results and eye diagrams for back-to-back, ○; 2 users, □; 4-users, ⋆ and 6 users, ◇; using (a) InP encoder and decoder chips, and (b) using SLPM encoders and decoder [44].

versus incorrectly decoded O-CDMA waveforms and an excellent match between theoretical predictions and experimental results.

Further, we have set up a two-time slotted, 6-user O-CDMA testbed experiment using the InP O-CDMA encoder and the InP O-CDMA decoder, and two SLPM-based encoders acting as interfering users (total of three encoders × two time slots).

Figure 15(a) shows the BER measurement results for the 2-, 4-, and 6-user OCDMA testbed with InP encoder and decoder [44]. The 2-user and 4-user experiments demonstrated error-free operation and a power penalty of 5.5 dB at BER = 10^{-9} with respect to back to back. The penalty can be mainly attributed to power lost from the ringing peaks. The 6-user case attained an error floor at 10^{-9}, primarily due to MUI inside the time gate. MUI effects are relatively small for 2 and 4 users, resulting in no observable noise floor. A narrower time gate window and/or longer code length would mitigate the MUI effects significantly and an error-free operation is expected.

To investigate the effect of the spectral filtering and loss in the InP based encoders–decoders, we repeated the BER measurement but replaced the InP devices with SLM based encoders–decoders. SLM devices approach ideal coding performance due to their rectangular filter shape. Figure 15(b) shows the BER measurement result and eye diagrams. The 2-user and 4-user experiments demonstrated error-free operation with a power penalty of 2 and 5 dB, respectively, at BER = 10^{-9}. The error floor below 10^{-9} in the 6-user SLM case confirms that MUI and not the InP chip response is the dominant limitation for error-free operation of O-CDMA system.

6.C. Differential MZI Threshold Detection

The final piece of the SPECT-OCDMA system for integration is the selective detection of correctly decoded O-CDMA signals while suppressing the incorrectly decoded interferer signals. Compared to previously shown fiber nonlinearity based thresholder approaches, the Mach–Zehnder interferometer (MZI) thresholder is less bulky, more sensitive, and compatible with monolithic integration with other semiconductor components. Here we describe an improved "clock-gated" MZI scheme with respect to the "self-gated" approach. Both schemes depend on differential operation of the MZI.

Figure 16 shows the self-gated and clock-gated MZI operation [45]. In the self-gated scheme, no external clock signal is provided. The decoded pulse is split in two and each part enters a distinct MZI arm with a time delay. Only the correctly decoded pulses have a sufficiently fast rising edge to saturate the nonlinear optical elements in

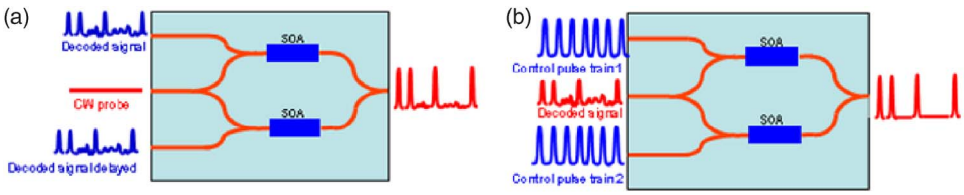

Fig. 16. OCDMA thresholder in (a) nongated, (b) clock-gated configuration.

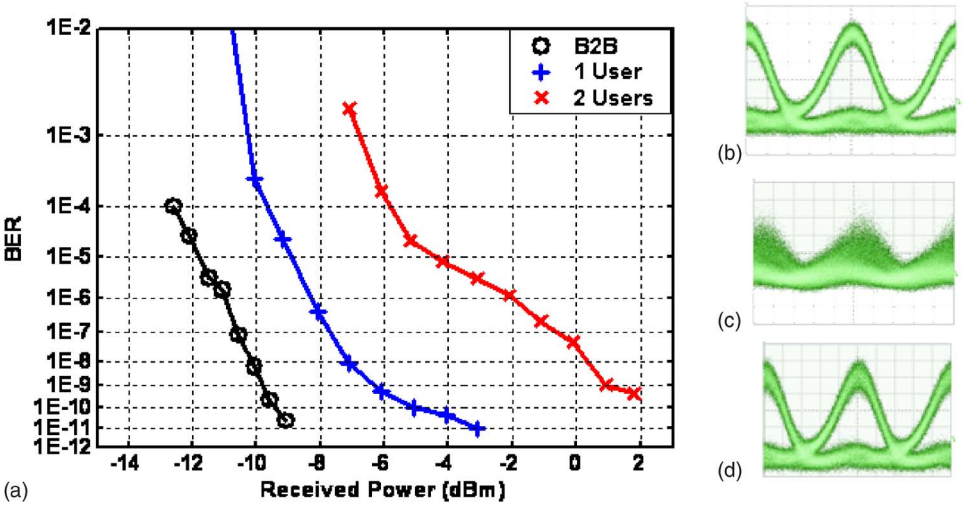

Fig. 17. Measured BER and electrical eye diagram for nongated scheme with 63-bit cyclically shifted *m*-sequence phase codes. (a) BER for back-to-back, 1-user, and 2-user cases. (b)–(d) are electrical eye diagrams for correctly decoded signal, incorrectly decoded signal, and 2-simultaneous user (correctly and incorrectly decoded users), respectively [47].

the MZI arms, opening a differential gate for the cw probe signal [46]. The clock-gated scheme uses the external short pulse clock signal for generating the differential gate of the MZI.

Figure 17 shows the BER results and the corresponding eye diagrams for the gated scheme using the SLPM-based testbed experiments with the 64-bit Walsh code based encoding and decoding [47]. The experiment utilized a $2^{23}-1$ PRBS. In this gated scheme, error-free operation and a clear eye opening were obtained for the correctly decoded signal (encoded and decoded with W5) and an error floor of 0.5 (off scale in the plot) and a closed eye for the incorrectly decoded (encoded with W5 and decoded with W34) signal. A clear open eye and a BER of less than 10^{-9} were also obtained for the correctly decoded user in the presence of an interferer [47].

7. Summary

This paper overviewed and summarized the progress of the SPECTS O-CDMA technology. The bulk optics testbed demonstrated a 320 Gbit/s (32-user $\times$ 10 Gbit/s) all-optical passive optical network based on the SPECTS O-CDMA technology. Ten gigabits per second CPM lasers with OSML capability, differential MZIs with threshold detection capability, and the AWG-PM array-AWG encoder–decoder for SPECTS O-CDMA encoding and decoding capability are key ingredients for the high-performance and low-cost O-CDMA microsystems monolithically integrated on an InP platform.

Acknowledgments

This work was supported in part by Defense Advanced Research Projects Agency (DARPA) and SPAWAR under agreement N66001-01-1 and by JOP-OIDA supported by DARPA and the National Science Foundation (NSF).

References

1. E. Park, A. J. Mendez, and E. M. Garmire, "Temporal/spatial optical CDMA networks—design, demonstration, and comparison with temporal networks," IEEE Photon. Technol. Lett. **4**, 1160–1162 (1992).
2. N. Wada and K. Kitayama, "A 10 Gb/s optical code division multiplexing using 8-chip optical bipolar code and coherent detection," J. Lightwave Technol. **17**, 1758–1765 (1999).
3. H. Fathallah, L. A. Rusch, and S. LaRochelle, "Passive optical fast frequency-hop CDMA communications system," J. Lightwave Technol. **17**, 397–405 (1999).
4. J. P. Heritage, R. N. Thurston, W. J. Tomlinson, A. M. Weiner, and R. H. Stolen, "Spectral

windowing of frequency-modulated optical pulses in a grating compressor," Appl. Phys. Lett. **47**, 87–89 (1985).
5. J. P. Heritage, A. M. Weiner, and R. N. Thurston, "Picosecond pulse shaping by spectral phase and amplitude manipulation," Opt. Lett. **10**, 609–611 (1985).
6. A. M. Weiner, J. P. Heritage, and E. M. Kirschner, "High-resolution femtosecond pulse shaping," J. Opt. Soc. Am. B **5**, 1563–1572 (1988).
7. A. M. Weiner, "Femtosecond pulse shaping using spatial light modulators," Rev. Sci. Instrum. **71**, 1929–1960 (2000).
8. A. M. Weiner, J. P. Heritage, and J. A. Salehi, "Encoding and decoding of femtosecond pulses," Opt. Lett. **13**, 300–302 (1988).
9. H. P. Sardesai, C. C. Chang, and A. M. Weiner, "A femtosecond code-division multiple-access communication system test bed," J. Lightwave Technol. **16**, 1953–1964 (1998).
10. H. Tsuda, H. Takenouchi, T. Ishii, K. Okamoto, T. Goh, K. Sato, A. Hirano, T. Kurokawa, and C. Amano, "Spectral encoding and decoding of 10 Gbit/s femtosecond pulses using high resolution arrayed-waveguide grating," Electron. Lett. **35**, 1186–1188 (1999).
11. Z. Zheng, S. Shen, H. Sardesai, C. C. Chang, J. H. Marsh, M. M. Karkhanehchi, and A. M. Weiner, "Ultrafast two-photon absorption optical thresholding of spectrally coded pulses," Opt. Commun. **167**, 225–233 (1999).
12. Z. Zheng and A. M. Weiner, "Spectral phase correlation of coded femtosecond pulses by second-harmonic generation in thick nonlinear crystals," Opt. Lett. **25**, 984–986 (2000).
13. S. Shen, A. M. Weiner, G. D. Sucha, and M. L. Stock, "Bit error rate performance of ultrashort-pulse optical CDMA detection under multi-access interference," Electron. Lett. **36**, 1795–1797 (2000).
14. R. M. Gagliardi and A. J. Mendez, "Pulse combining and time-space coding for multiple accessing with fiber arrays," presented at the IEEE/LEOS Summer Topical Meeting on Optical Multiple Access Networks, Monterey, Calif., 25–27 July, 1990.
15. A. J. Mendez, J. L. Lambert, J. M. Morookian, and R. M. Gagliardi, "Synthesis and demonstration of high speed, bandwidth efficient optical code division multiple access (CDMA) tested at 1 Gb/s throughput," IEEE Photon. Technol. Lett. **6**, 1146–1149 (1994).
16. N. Karafolas and D. Uttamchandani, "Optical fiber code division multiple access networks: a review," Opt. Fiber Technol. **2**, 149–168 (1996).
17. K. Iversen, J. Muckenheim, and D. Hampicke, "A basic theory of fiber-optic CDMA," presented at the IEEE 4th International Symposium on Spread Spectrum Techniques and Applications, Mainz, Germany, 22–25 Sept. 1996.
18. K. Iversen and D. Hampicke, "Comparison and classification of all-optical CDMA systems for future telecommunication networks," Proc. SPIE **2644**, 110–121 (1995).
19. D. D. Sampson, G. J. Pendock, and R. A. Griffin, "Photonic code-division multiple-access communications," Fiber Integr. Opt. **16**, 129–157 (1997).
20. P. R. Prucnal ed., *Optical Code Division Multiple Access: Fundamentals and Applications* (Taylor & Francis, 2006).
21. Z. Jiang, S.-D. Yang, D. E. Leaird, and A. M. Weiner, "Fully dispersion-compensated ~500 fs pulse transmission over 50 km single-mode fiber," Opt. Lett. **30**, 1449–1451 (2005).
22. S. Shen and A. M. Weiner, "Complete dispersion compensation for 400 fs pulse transmission over 10 km fiber link using dispersion compensating fiber and spectral phase equalizer," IEEE Photon. Technol. Lett. **11**, 827–829 (1999).
23. C. Ji, R. G. Broeke, Y. Du, C. Jing, N. Chubun, P. Bjeletich, F. Olsson, S. Lourdudoss, R. Welty, C. Reinhardt, P. L. Stephan, and S. J. B. Yoo, "Monolithically integrated InP-based photonic chip development for O-CDMA systems," IEEE J. Sel. Top. Quantum Electron. **11**, 66–77 (2005).
24. J. Cao, R. G. Broeke, N. Fontaine, W. Cong, C. Ji, Y. Du, N. Chubun, K. Aihara, A.-V. Pham, J. P. Heritage, B. H. Kolner, S. J. B. Yoo, F. Olsson, S. Lourdudoss, and P. L. Stephan, "Error-free spectral encoding and decoding operation of InP O-CDMA encoder," presented at the Optical Fiber Communications Conference, Anaheim, California, USA, 5–10 Mar. 2006.
25. W. Cong, C. Yang, R. P. Scott, V. J. Hernandez, N. K. Fontaine, B. H. Kolner, J. P. Heritage, and S. J. B. Yoo, "Demonstration of 160- and 320-Gb/s SPECTS O-CDMA Network Testbeds," IEEE Photon. Technol. Lett. **18**, 1567–1569 (2006).
26. X. Wang and K. Kitayama, "Analysis of beat noise in coherent and incoherent time-spreading OCDMA," J. Lightwave Technol. **22**, 2226–2235 (2004).
27. V. J. Hernandez, C. Wei, H. Junqiang, Y. Chunxin, N. K. Fontaine, R. P. Scott, D. Zhi, B. H. Kolner, J. P. Heritage, and S. J. B. Yoo, "A 320-Gb/s capacity (32-user 10 Gb/s) SPECTS O-CDMA network testbed with enhanced spectral efficiency through forward error correction," J. Lightwave Technol. **25**, 79–86 (2007).
28. C. Wei, Y. Chunxin, R. P. Scott, V. J. Hernandez, N. K. Fontaine, B. H. Kolner, J. P. Heritage, and S. J. B. Yoo, "Demonstration of 160- and 320-Gb/s SPECTS O-CDMA network testbeds," IEEE Photon. Technol. Lett. **18**, 1567–1569 (2006).
29. C. Wei, Y. Chunxin, R. P. Scott, V. J. Hernandez, N. K. Fontaine, J. P. Heritage, B. H. Kolner, and S. J. B. Yoo, "A sixteen-user time-slotted SPECTS O-CDMA network testbed," presented at Optical Fiber Communication Conference and National Fiber Optic Engineers Conference, Anaheim, California, USA, 5–10 Mar. 2006.
30. L. Nguyen, T. Dennis, B. Aazhang, and J. F. Young, "Optical spectral amplitude CDMA communication," J. Lightwave Technol. **15**, 1647–1653 (1997).
31. Y. Du, S. J. B. Yoo, and Z. Ding, "Nonuniform spectral phase encoding in optical CDMA networks," IEEE Photon. Technol. Lett. **18**, 2505–2507 (2006).
32. E. J. Skogen, J. W. Raring, G. B. Morrison, C. S. Wang, V. Lal, M. L. Masanovic, and L. A.

Coldren, "Monolithically integrated active components: a quantum-well intermixing approach," IEEE J. Sel. Top. Quantum Electron. **11**, 343–355 (2005).
33. Y. K. Chen, M. C. Wu, T. Tanbun-Ek, R. A. Logan, and M. A. Chin, "Subpicosecond monolithic colliding-pulse mode-locked multiple quantum well lasers," Appl. Phys. Lett. **58**, 1253–1255 (1991).
34. Y.-K. Chen and M. C. Wu, "Monolithic colliding-pulse mode-locked quantum-well lasers," IEEE J. Quantum Electron. **28**, 2176–2185 (1992).
35. C. Ji, R. G. Broeke, Y. Du, J. Cao, N. Chubun, P. Bjeletich, F. Olsson, S. Lourdudoss, R. Welty, C. Reinhardt, P. L. Stephan, and S. J. B. Yoo, "Monolithically integrated InP-based photonic chip development for O-CDMA systems," IEEE J. Sel. Top. Quantum Electron. **11**, 66–77 (2005).
36. K. Yvind, D. Larsson, L. J. Christiansen, J. Mork, J. M. Hvam, and J. Hanberg, "High-performance 10 GHz all-active monolithic modelocked semiconductor lasers," Electron. Lett. **40**, 735–737 (2004).
37. C. Ji, N. Chubun, R. G. Broeke, J. Cao, Y. Du, T. Tekin, S. J. B. Yoo, K. Y. Liou, J. R. Lothian, S. Vatanapradit, S. N. G. Chu, B. Patel, W. S. Hobson, D. V. Tishinin, and W. T. Tsang, "10 GHz colliding pulse mode-locked laser with electrical and optical injection synchronization," presented at the 2005 IEEE LEOS Annual Meeting, Sydney, New South Wales, Australia, 22–28 Oct. 2005.
38. C. Ji, N. Chubun, R. Broeke, J. Cao, Y. Du, and S. J. B. Yoo, "Synchronization of InP colliding pulse mode-locked laser by electrical subharmonic modulation," presented at the 2004 IEEE LEOS Annual Meeting, Rio Grande, Puerto Rico, 10–11 Nov. 2004.
39. C. Ji, N. Chubun, R. G. Broeke, J. Cao, Y. Du, P. Bjeletich, and S. J. B. Yoo, "Electrical subharmonic hybrid mode locking of a colliding pulse mode-locked laser at 28 GHz," IEEE Photon. Technol. Lett. **17**, 1381–1383 (2005).
40. S. Arahira and Y. Ogawa, "480-GHz subharmonic synchronous mode-locking in a short-cavity colliding-pulse mode-locked laser diode," IEEE Photon. Technol. Lett. **14**, 537–539 (2002).
41. H. Kurita, T. Shimizu, and H. Yokoyama, "Experimental investigations of harmonic synchronization conditions and mechanisms of mode-locked laser diodes induced by optical-pulse injection," IEEE J. Sel. Top. Quantum Electron. **2**, 508–513 (1996).
42. R. Trebino, *Frequency-Resolved Optical Gating: The Measurement of Ultrashort Laser Pulses* (Kluwer Academic, 2000).
43. C. Ji, N. Chubun, R. G. Broeke, J. Cao, Y. Du, S. J. B. Yoo, K. Y. Liou, J. R. Lothian, S. Vatanapradit, S. N. G. Chu, B. Patel, W. S. Hobson, and W. T. Tsang, "Synchronized transform-limited operation of 10 GHz colliding pulse mode-locked laser," IEEE Photon. Technol. Lett. **18**, 625–627 (2006).
44. J. Cao, R. G. Broeke, N. Fontaine, C. Ji, Y. Du, N. Chubun, K. Aihara, A.-V. Pham, F. Olsson, S. Lourdudoss, and S. J. B. Yoo, "Demonstration of spectral phase O-CDMA encoding and decoding in monolithically integrated arrayed-waveguide-grating-based encoder," IEEE Photon. Technol. Lett. **18**, 2602–2604 (2006).
45. Y. Du, T. Tekin, R. G. Broeke, N. Chubun, C. Ji, J. Cao, S. J. B. Yoo, K. Y. Liou, J. R. Lothian, S. Vatanapradit, S. N. G. Chu, B. Patel, W. S. Hobson, D. V. Tishinin, and W. T. Tsang, "A novel monolithically integrated Mach–Zehnder wavelength converter using cross modulation in electro-absorber," presented at the 31st European Conference on Optical Communication, Glasgow, UK, 25–29 Sept. 2005.
46. T. Durhuus, C. Joergensen, B. Mikkelsen, R. J. S. Pedersen, and K. E. Stubkjaer, "All-optical wavelength conversion by SOAs in a Mach–Zehnder configuration," IEEE Photon. Technol. Lett. **6**, 53–55 (1994).
47. Y. Du, J. Cao, and S. J. B. Yoo, "Performance comparison of gated and nongated all-optical thresholding detection schemes using Mach–Zehnder interferometers in SPECTS O-CDMA," IEEE Photon. Technol. Lett. **19**, 1054–1056 (2007).